



Revealing orbital texture of grey arsenic through linear dichroism in multidimensional photoemission spectroscopy



Jingwei Dong^{1,2,8}, Jiuxiang Zhang^{3,8}, Zailan Zhang^{4,8}, Dan Luo^{1,2}, Yongguang Zhang^{1,2}, Zhesheng Chen⁵, Runze Liu⁶ ✉, Azzedine Bendounan⁷ ✉ & Zhongwei Chen^{1,2} ✉

Two-dimensional (2D) layered material grey arsenic exhibits great potential for electronic and optoelectronics devices. Identifying the orbital texture in the electronic energy bands close to Fermi level is crucial for understanding and further manipulating the optoelectronic properties of grey arsenic. In this work, we investigate the orbital properties from bulk-state and surface-state of grey arsenic by using multidimensional angle-resolved photoemission spectroscopy, under different light polarization and crystal orientation conditions. Furthermore, by combining the experimental results with first-principles calculations based on density functional theory (DFT), we reveal that both the surface and bulk states of grey arsenic contain 4s, $4p_x$, $4p_y$ and $4p_z$ orbitals, but the orbital ratios are different. Our study offers new insight into the orbital nature of grey arsenic and also paves the way for investigation of orbital properties in other 2D materials.

Van der Waals (vdW) layered materials have been investigated intensively due to their outstanding properties which are relevant to diverse applications including next-generation computing, efficient optoelectronic devices, energy conversion and storage technologies^{1,2}. Arsenic stands out among the elements due to its ability to manifest diverse allotropes, especially in layered structures. This characteristic makes arsenic an exceptionally promising candidate for a wide array of applications, ranging from field-effect transistors, sensors to catalysts^{3,4}. Grey arsenic, characterized by its covalently bonded and layered structure in the rhombohedral phase, represents the most prevalent and stable crystal structure of arsenic at room temperature. The distinctive electronic structural attributes of grey arsenic are key contributors to a myriad of intriguing optical and electronic phenomena. The arsenic electron configuration is $1s^2 2s^2 2p^6 3s^2 3p^6 4s^2 3d^{10} 4p^3$. Notably, the existence of cross-layer orbitals within grey arsenic results in a strong interlayer bonding energy, culminating in semimetallic behavior and high conductivity⁵. The surface band is of conventional Shockley type, and the

spin of surface states are locked to their momentum at low energies while the surface band has a significant out-of-plane spin component at the higher-energy part^{6,7}. Furthermore, the unique bulk-surface-edge states observed by Hossain et al.⁸ suggest that grey arsenic can be used as a platform for studying quantum information science in future devices. The electronic states proximate to the Fermi level intricately shape the optical and electronic properties of the conducting materials, as the migration of electrons during various physical and chemical processes primarily occurs in the vicinity of the Fermi level^{9,10}. The orbital texture of both bulk and surface states is vital to understand the device performance based on grey arsenic. Despite extensive studies have been focused on the optoelectronic characteristics of grey arsenic, direct investigation on the orbital texture of this material remains elusive so far.

Angle-resolved photoemission spectroscopy (ARPES) stands as a powerful technique in probing the electronic band structure of solid materials, accompanying with both ultrahigh energy and momentum

¹Power Battery & Systems Research Center, Dalian Institute of Chemical Physics, Chinese Academy of Sciences, Dalian, 116023, PR China. ²State Key Laboratory of Catalysis, Dalian Institute of Chemical Physics, Chinese Academy of Sciences, Dalian, 116023, PR China. ³Beijing National Laboratory for Condensed Matter Physics, Institute of Physics, Chinese Academy of Sciences, Beijing, 100190, PR China. ⁴School of Physics, Nanjing University of Science and Technology, Nanjing, 210094, PR China. ⁵School of Materials Science and Engineering, Nanjing University of Science and Technology, Nanjing, 210094, PR China. ⁶School of Science, Dalian Jiaotong University, Dalian, 116028, PR China. ⁷Société Civile Synchrotron SOLEIL, L'Orme des Merisiers, Départementale 128, Saint-Aubin, 91190, France. ⁸These authors contributed equally: Jingwei Dong, Jiuxiang Zhang, Zailan Zhang. ✉e-mail: rzliu@sdu.edu.cn; azzedine.bendounan@synchrotron-soleil.fr; zwchen@dicp.ac.cn

resolutions. Similar to the scanning tunneling microscopy and resonant inelastic X-ray scattering, ARPES can potentially provide a way to reveal the orbital characteristics of electronic states^{11–13}. During ARPES measurements, by manipulating the experimental geometry between light and sample, for example the in-plane orientation and polarization of the light, one can distinguish the orbital texture in the measured bands, which has been applied in many materials^{14–17}. It is well known that the transition dipole matrix element largely affects the intensity of the ARPES spectra, which leads to discrepancies between ARPES spectral lineshapes and spectral functions¹⁸. The matrix element effects comprise two primary contributions: the intrinsic factor stemming from the nature of the initial state of emitted electrons and the extrinsic factor involving experimental geometry, such as light polarization, photon momentum and crystal orientation. Given that the final state is an even function, the orbital nature can be probed by aligning the orbital with the light polarization in the plane of the photoelectron energy analyzer according to selection rule in photoemission process. For instance, strategic manipulation of crystal rotation and light polarization during measurements allows for the selective suppression or enhancement of photoelectron yield from specific electronic states, thereby unveiling the orbital characteristics of the initial state^{19–24}.

In this work, we investigate the modulation of photoemission intensity in high-quality single crystals of grey arsenic upon sample rotation and light polarization by using ARPES. In the Fermi surface map, anisotropic photoelectron intensity is directly observed in grey arsenic. By rotating the in-plane azimuth angle of the sample, we observe the ARPES signal rotating simultaneously under both p and s polarization of light, which indicates the intrinsic dichroism in grey arsenic. The orbital nature of bulk states and surface states was further explored by the band structure calculated from first-principles theory. Our results could potentially facilitate the design of multifunctional optoelectronic devices based on grey arsenic.

Results

Basic properties of grey arsenic and experimental setup

The bulk Brillouin zone (BZ) and projected surface Brillouin zone (SBZ) of grey arsenic with the labeled high-symmetry points and directions are shown in Fig. 1a. Grey arsenic has a rhombohedral primitive cell with space group of $R\bar{3}m$ (No. 166). Notably, the 3-fold rotational symmetry of the grey arsenic crystal structure dictates a 60° angular difference between two nearest $\bar{\Gamma}$ - \bar{M} and $\bar{\Gamma}$ - \bar{M}' . For inversion symmetric crystal like grey arsenic, a 60° crystal rotation is equivalent to a mirror-image symmetry for the (111) surface (see the lower right corner of Fig. 1b, which displays the schematic of the experimental geometry referred to the (111) surface for disentangling extrinsic and intrinsic contributions in the ARPES measurements of the orbital texture of grey arsenic). Besides, the photon scattering plane and crystal directions are shown in Fig. 1b. Here the photon scattering plane overlaps with the photoemission mirror plane. In addition to the photoemission mirror plane, the grey arsenic crystal also has its own crystal mirror planes. For example, the two crystal mirror planes are shown in the lower right corner of Fig. 1b. The photon scattering plane is perpendicular to the crystal mirror plane. We characterized the quality of the sample by using X-ray photoelectron spectroscopy (XPS) under the photon energy of 130 eV, as shown in Fig. 1c. It is worth noting that the valence bands, 4p and 3d core levels of grey arsenic have sharp features, and the spin-orbit splitting states of As 3d core levels can be clearly discerned by the fitting with the mixture of Gaussian and Lorentzian functions under a ratio of 80%G and 20%L. The theoretical studies of Zhang⁶ and Yoshizawa²⁵ suggest that the hybrid orbitals near the Fermi level may consist of 4s and 4p atomic orbitals of grey arsenic. In our work, we further investigate the properties of such hybrid orbitals by combining ARPES and DFT calculations. Figure 1d illustrates the correlation between the scattering plane and the spatial symmetry of various atomic orbitals (s, p_x, p_y , and p_z) projected onto the (111) crystal surface. In Fig. 1e, the entire band structure along the \bar{M} - $\bar{\Gamma}$ - \bar{M}' high symmetry direction are

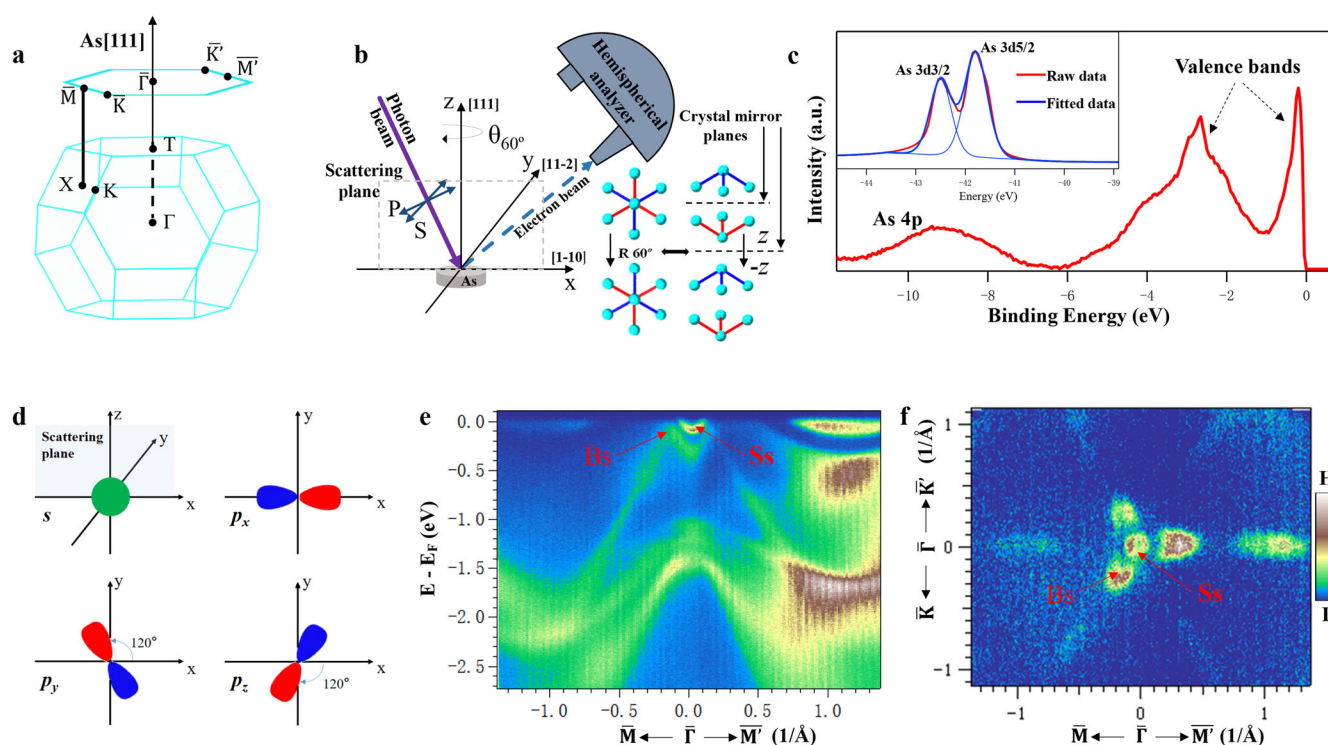


Fig. 1 | Basic properties of grey arsenic. **a** Bulk BZ and (111) surface BZ with indexes on the high-symmetry points. **b** Scheme of the multidimensional photoemission spectroscopy experiments. The coordinate system corresponds to the laboratory frame. The schematic in the lower right corner represents the equivalent operation between a crystal rotation by 60° ($R60^\circ$, top view) in the laboratory frame and a mirror symmetry ($z \rightarrow -z$) in grey arsenic. The black dotted lines indicate the

crystal mirror planes. **c** High resolution X-ray photoelectron spectroscopy (XPS) spectra of As 3d (inset Fig.), As 4p and valence bands. **d** Projection of the p and s orbitals onto the (111) surface. **e** ARPES of grey arsenic along the \bar{M} - \bar{M}' high symmetry direction acquired under photon energy of 70 eV and p polarization. **f** The entire Fermi surface map of grey arsenic taken under photon energy of 120 eV and p polarization. The Ss and Bs represent the surface states and bulk states, respectively.

obtained from ARPES under photon energy of 70 eV and p polarization. The band structure of grey arsenic exhibits considerable similarity with the ones of antimony and bismuth²⁶. Additionally, the entire Fermi surface map (constant energy contour (CEC) at the Fermi level ($E - E_F = 0$ eV)) of grey arsenic is shown in Fig. 1f. It can be seen from the Fermi surface map that the band structure of grey arsenic holds three-fold rotational symmetry in momentum space while the intensity of the bands is not homogeneous, which calls for a detailed discussion in the following.

In our experimental geometry (see Fig. 1b), the p-polarized light manifests an incoming electric field lying within the scattering plane (XZ), signifying the even nature of p polarization under the reflection with respect to the scattering plane. Conversely, s-polarized light has an incoming electric field perpendicular to the scattering plane, which demonstrates the odd symmetry of s polarization in terms of the scattering plane. Thus, s orbitals can be detected by p-polarized light but not by s-polarized light. Table 1 presents a comprehensive summary of the overall matrix elements of the p orbitals when the $\bar{M}-\bar{\Gamma}-\bar{M}'$ or $\bar{K}-\bar{\Gamma}-\bar{K}'$ direction of the crystal is within the scattering plane.

Intrinsic linear dichroism in photoelectron angular distributions

The intrinsic origins (orbital symmetry/orientation) and extrinsic factors (experimental geometry) can be distinguished by the extraction of the

intrinsic linear dichroism in photoelectron angular distributions (iLDAD) based on ARPES measurements on the orbital texture, according to the previous reports by Beaulieu et al.^{19,27}. Figure 2 highlights the analysis of iLDAD from two crystal orientation rotated by 60° relative to each other. In Fig. 2, the bulk states and surface states are clearly seen from the Fermi surface maps of ARPES data. Around $\bar{\Gamma}$, the surface states exhibit slight angular anisotropy for the photoemission intensity. However, one can see notable asymmetry in photoelectron yield of surface states and bulk states between \bar{M} and \bar{M}' , where the photoemission intensity is much stronger around \bar{M}' compared to \bar{M} within our measured momentum range, as shown in the Fermi surface map of Fig. 2a. The pronounced angular anisotropies should be related to the symmetry properties of the orbitals, which can also be observed after a 60° azimuthal rotation, as shown in Fig. 2b.

The conformation of orbital factors necessitates the elimination of experimental geometry contributions from the antisymmetric signal of the Fermi surface maps acquired by p-polarized light. The linear dichroism asymmetry in the photoelectron angular distribution $A_{LDAD}^a(E, k_x, k_y)$ can be extracted from the normalized photoemission intensity difference between the forward map ($I_a(E, k_x, k_y)$) and backward map ($I_a(E, -k_x, k_y)$) (see Eq. (1)). And to unveil the orbital texture of grey arsenic, the intrinsic linear dichroism in photoelectron angular distributions iLDAD (i.e., $(A_{LDAD}^a - A_{LDAD}^{a'})/2$, with $a - a' = 60^\circ$) is also introduced as the ref. 19.

$$A_{LDAD}^a = \frac{I_a(E, k_x, k_y) - I_a(E, -k_x, k_y)}{I_a(E, k_x, k_y) + I_a(E, -k_x, k_y)} \quad (1)$$

The results are shown in Fig. 2c, d and e, respectively, in which the intrinsic orbital symmetry/orientation influences the asymmetric photoemission intensities, as demonstrated by both $A_{LDAD}^{0^\circ}$ and $A_{LDAD}^{60^\circ}$. The extrinsic contribution is negligible, as the dichroic signal keeps almost the same under such operation^{25,28}. The iLDAD further supports that the

Table 1 | Detectability of 4p orbitals along two high symmetry directions with p and s polarization light ARPES

High symmetry direction	Light polarization	4p orbitals		
		p_x	p_y	p_z
$\bar{M}-\bar{\Gamma}-\bar{M}'$	p	Yes	Yes	Yes
	s	No	Yes	Yes
$\bar{K}-\bar{\Gamma}-\bar{K}'$	p	Yes	No	Yes
	s	Yes	Yes	Yes

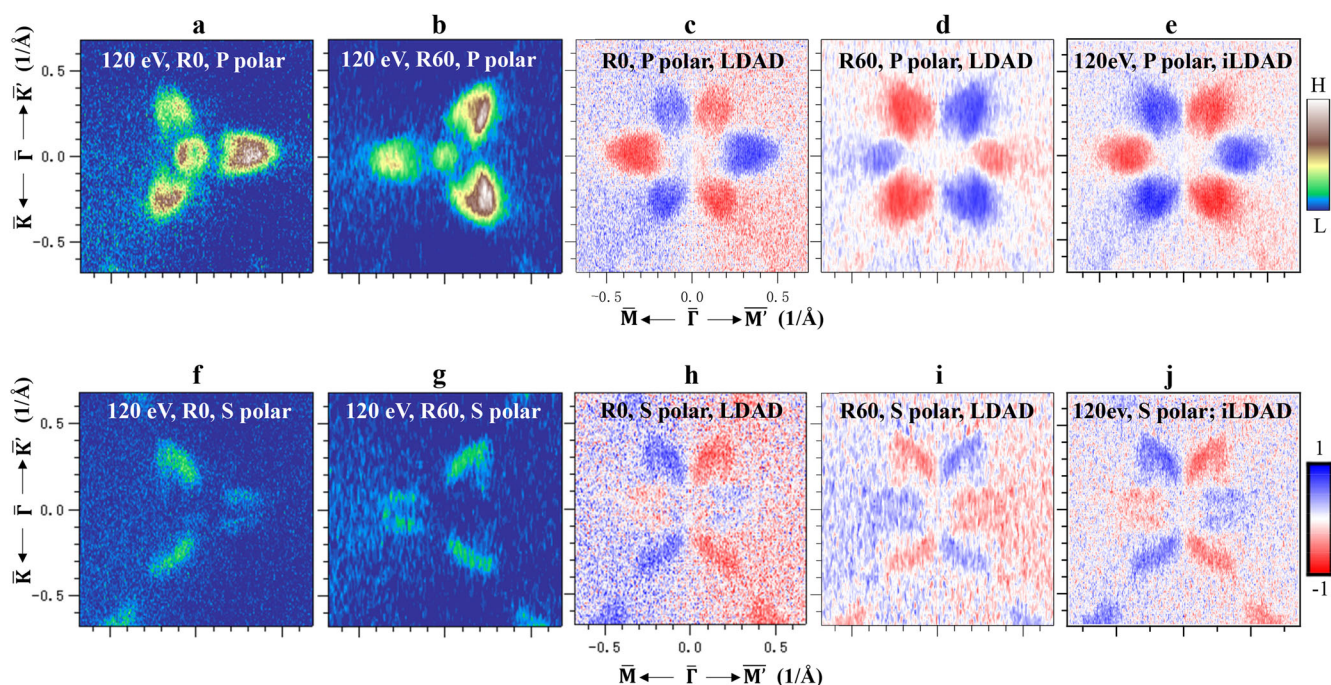


Fig. 2 | Extraction of intrinsic linear dichroism in photoelectron angular distributions (iLDAD) by p and s polarized light with photon energy of 120 eV. Panels (a) and (b) display the CECs at the Fermi level ($E - E_F = 0$ eV) obtained from measurements conducted on two crystal orientations rotated by 60° with respect to each other using p polarized light; (c) and (d) show R0-LDAD and R60-LDAD,

representing the “left-right asymmetries”, indicating the photoemission intensity asymmetry between the negative momentum and positive momentum hemispheres for the respective crystal orientations; (e) iLDAD illustrates the component of $A_{LDAD}^{R0/R60}$ exhibiting antisymmetry upon a 60° azimuthal rotation of the sample; (f-j) the corresponding signals obtained using s-polarized light.

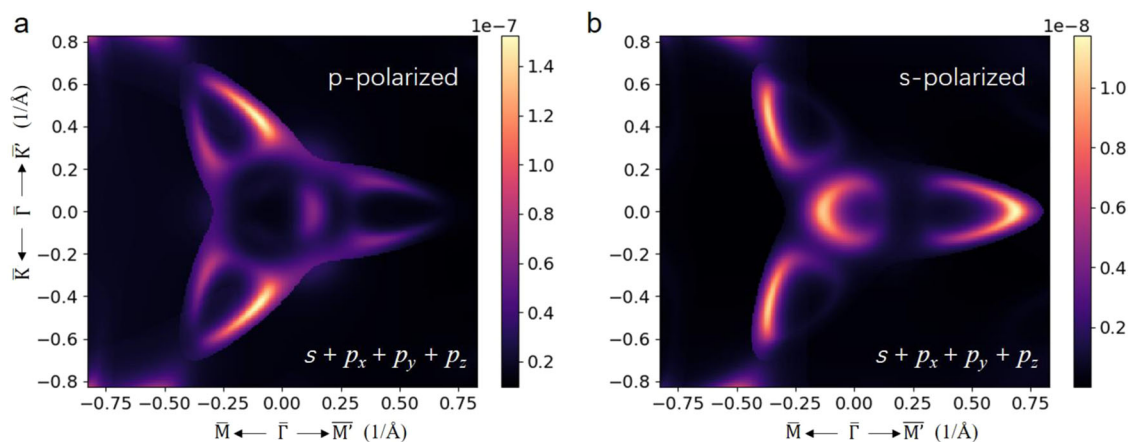


Fig. 3 | Calculated constant energy contours at the Fermi energy for grey arsenic via chinook code with the basis including 4s and 4p orbitals. Panels (a) and (b) are CECs obtained using p- and s-polarized light, respectively.

observed anisotropies stem from the intrinsic origins. It is essential to highlight that within p-polarized light, the maintenance of up/down symmetry is expected. However, after a 60-degree rotation, the dichroic signal of surface states becomes weaker compared to bulk states, which can be attributed to experimental imperfections within crystal orientation, optical beam alignment, or photoelectron imaging. Applying the same procedure described above to the CECs obtained with s-polarized light reveals similar anisotropic photoemission intensities between \bar{M} and \bar{M}' (see Fig. 2f–j). This similarity underscores the intrinsic contribution, indicating parity symmetry of the initial states. The difference of photoemission intensities between p-polarized and s-polarized light results from the extrinsic origin stemming from the orthogonal incident electric field distribution to each other (see Fig. 1b).

Furthermore, to gain insights into the orbital texture from the observed anisotropies of CECs, we conducted a tight-binding (TB) calculation using the chinook code. In this model, we explicitly include the arsenic 4s and 4p orbitals for the basis set, and the Hamiltonian is constructed using the Slater-Koster formalism. Both s- and p-polarized light were carefully considered in the simulation to properly account for their effects on the photoemission process. This approach allows us to capture the orbital texture and the orbital contributions for the formation of iLDAD. As shown in Fig. 3, the CECs using the photon energy of 120 eV obtained from the TB model exhibits good agreement with the experimental APRES data. As from Fig. 3, the calculated constant energy contour shows a clear asymmetry for photoelectron angular distribution of the surface and bulk states towards different high-symmetry directions, which corresponds to the dichroism. Moreover, the photoemission response exhibits dependence on photon polarization, and p-polarized light producing stronger intensity, in agreement with the experimental findings. To further elucidate the role of individual orbitals in photoemission, we performed additional calculations to assess their contributions to the photoelectron angular distributions. In the Figs. S3–S7, we present CECs obtained from TB models that include different orbital combinations of arsenic 4s, 4p_x, 4p_y, and 4p_z orbitals under varying light polarization conditions. Figure S3 shows the CEC obtained without the inclusion of 4s orbitals. Comparing this with Fig. 3, we find no significant difference in distribution patterns, except for a minor intensity decrease. This result indicates that 4s orbitals contribute minimally to the dichroism of the arsenic system, while the three p orbitals (4p_x, 4p_y, and 4p_z) play a crucial role in the formation of iLDAD.

Figures S4–S6 illustrate the CESs calculated without the contribution of 4p_x, 4p_y, and 4p_z, respectively. The resulting patterns exhibit significant discrepancies compared to the full 4s-4p model, highlighting that each of the three p orbitals plays a distinct role in shaping the photoelectron angular distribution. Noted that we do not observe a one-to-one correspondence between a specific orbital (4p_x, 4p_y, and 4p_z) and a particular direction in

momentum space, indicating that the contributions from the p orbitals are highly coupled. Their differing responses to the p- and s-polarized photons also provide clear evidence of the impact of light polarization on the photoelectron angular distribution. We further provide the contributions of single 4p_x, 4p_y, and 4p_z orbital on the photoelectron angular distribution, which are shown in Figs. S7–S9.

Orbital excitations with linearly polarized photons

In addition, we measured the band structure using p-polarized and s-polarized light along the \bar{M} - $\bar{\Gamma}$ - \bar{M}' and \bar{K} - $\bar{\Gamma}$ - \bar{K}' high-symmetry directions, respectively (see Fig. 4). Figure 4a, b depicts the band structure and $A_{\text{LDAD}}^0(E, k_x, 0)$ of grey arsenic along the \bar{M} - $\bar{\Gamma}$ - \bar{M}' direction with p-polarized light, respectively. These figures show pronounced photoemission anisotropies in both bulk valence band and surface band between positive and negative momentum. Since bulk valence band and surface band can be measured with p polarized light, these states might consist of orbitals with even nature (s and p_x) and non-symmetry orbitals (p_y and p_z) with respect to the scattering plane. As shown in Fig. 4c and d, upon switching the polarization from p to s, the strong photoemission anisotropies are still observable. This observation implies that both surface states around $\bar{\Gamma}$ and bulk states around \bar{M} and \bar{M}' points close to the Fermi level might contain p_y and p_z orbitals because of their odd nature. Remarkably, the anisotropy of surface states by s-polarized light is completely opposite to that observed in p-polarized photoemission spectroscopy, while the anisotropy of bulk states remains consistent. We consider that the observed discrepancies in photoemission anisotropies between surface and bulk states stem from distinct orbital hybridization, correlated with the momentum-dependent orbital texture and the emergence of strong intrinsic linear dichroism in the photoelectron angular distributions. Corresponding results along the \bar{K} - $\bar{\Gamma}$ - \bar{K}' direction are shown in Fig. 4e–h, respectively. In spite of differences in high-symmetry directions, we observe notable photoemission anisotropies in both surface and bulk states between positive and negative momentum. The striking asymmetry around \bar{M}/\bar{M}' and \bar{K}/\bar{K}' points for bulk states and $\bar{\Gamma}$ point of surface states close to the Fermi level in the momentum space should be mainly contributed from the As-4p hole pockets and the As-4p electron pockets, respectively. It is worth noting that both the surface states and bulk states exhibit the possible contributions from 4s, 4p_x, 4p_y, and 4p_z orbital.

To analyze the orbital texture of surface and bulk states in grey arsenic quantitatively, energy distribution curves (EDCs, Fig. 5) are obtained by integration around $\bar{\Gamma}$ (k_{\parallel} : -0.05 to 0.05 Å⁻¹, E: 0 to -0.35 eV; surface states), \bar{M} (k_{\parallel} : -0.40 to -0.20 Å⁻¹, E: 0 to -1.50 eV; bulk states) along \bar{M} - $\bar{\Gamma}$ - \bar{M}' direction and \bar{K} (k_{\parallel} : -0.40 to -0.20 Å⁻¹, E: 0 to -1.50 eV; bulk states) along \bar{K} - $\bar{\Gamma}$ - \bar{K}' direction from Fig. 4a, c, e and g, respectively. The normalized EDCs of the surface and bulk states vary with high symmetry directions and light

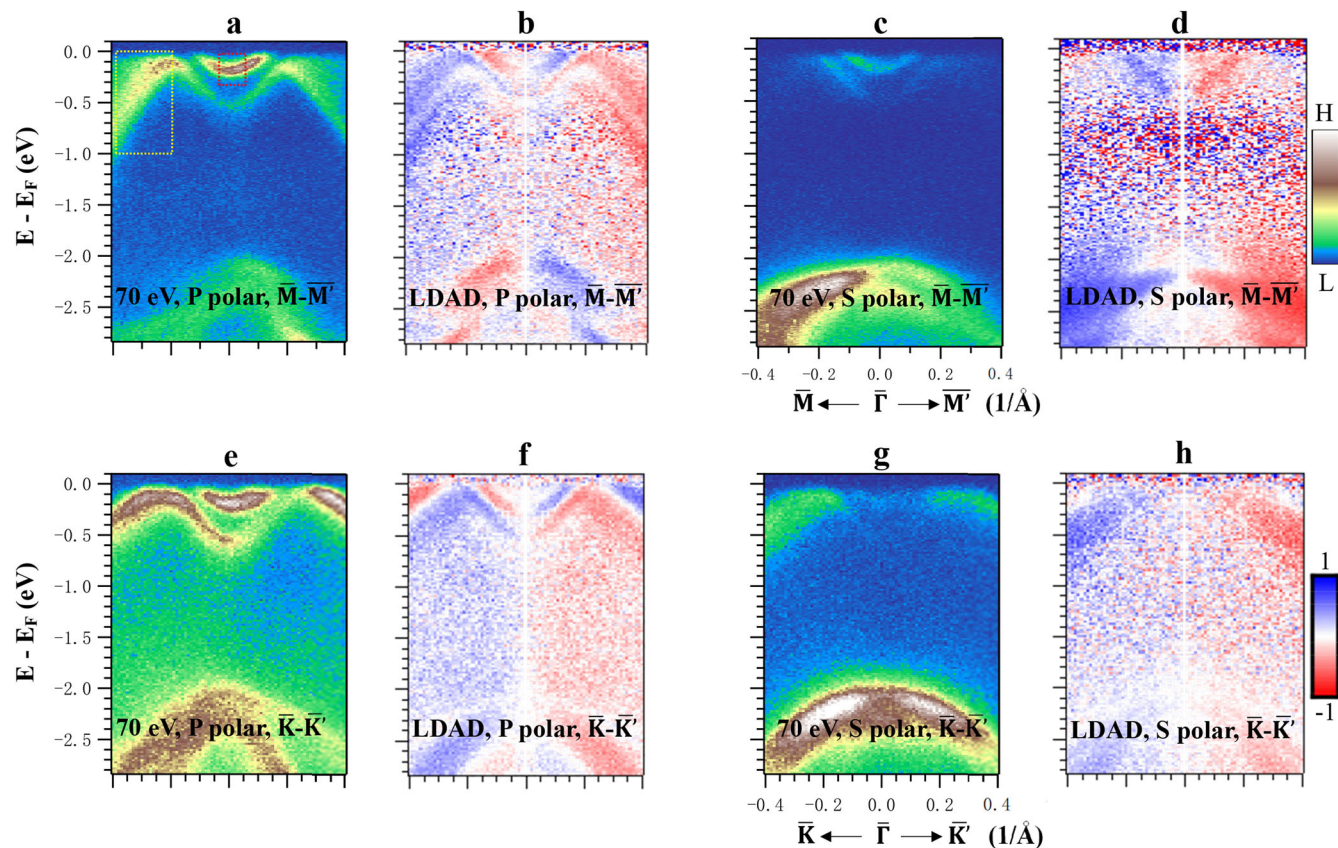


Fig. 4 | Band structure and corresponding LDAD of grey arsenic cuts using 70 eV light with p and s polarization. a Band structure acquired by p-polarized photon along $\bar{M}-\bar{\Gamma}-\bar{M}'$. The red and yellow dashed squares represent the integration range of the surface and bulk states for extracting energy distribution curves. b The LDAD of

the band structure along $\bar{M}-\bar{\Gamma}-\bar{M}'$ using p-polarized photon. c Band structure obtained by s-polarized photon along $\bar{M}-\bar{\Gamma}-\bar{M}'$. d The LDAD of the band structure along $\bar{M}-\bar{\Gamma}-\bar{M}'$ using s-polarized photon. e-g Similar measurements and representations for the $\bar{K}-\bar{\Gamma}-\bar{K}'$ direction.

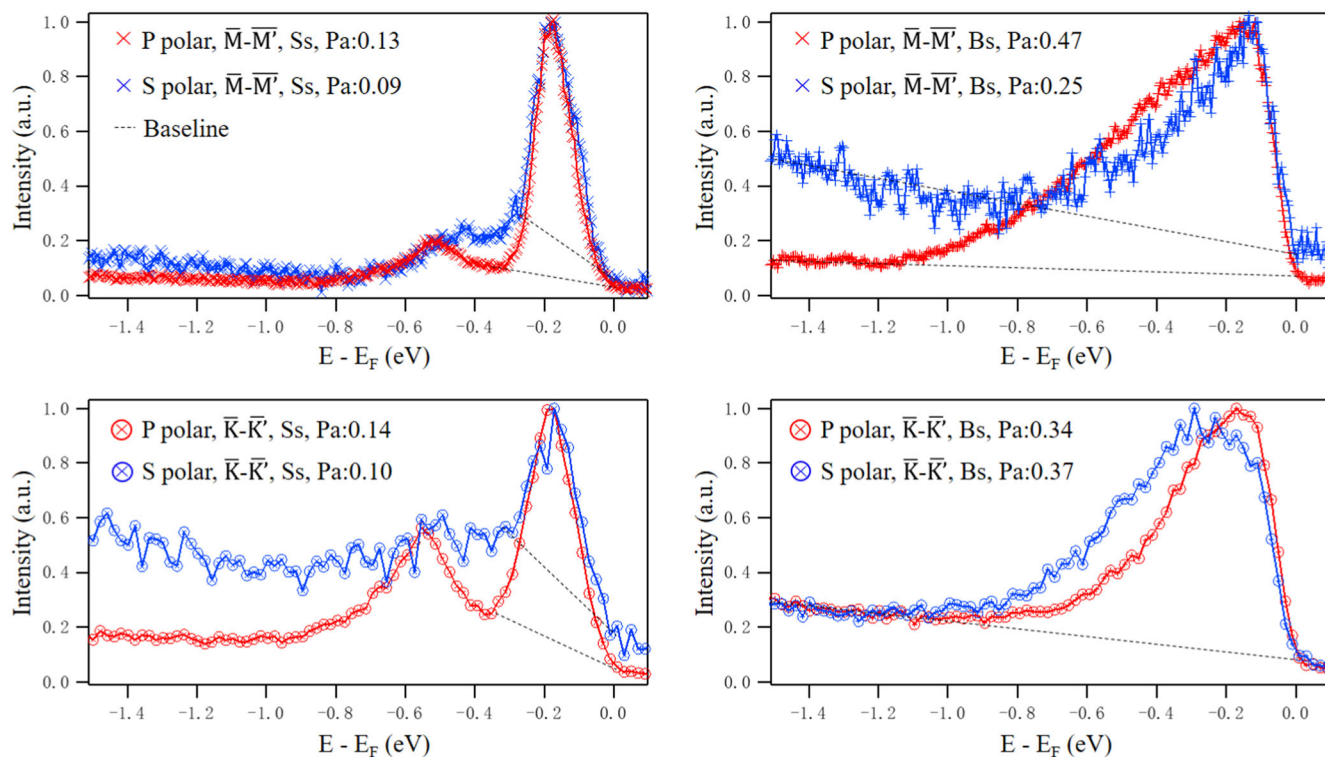


Fig. 5 | Momentum-integrated EDCs from Fig. 4a, c, e and g. Light polarization are indicated in each graph. Pa represents peak area. All the EDCs are normalized and the extracted peak areas are acquired by subtracting baselines.

polarization. For example, along $\bar{M}-\bar{\Gamma}-\bar{M}'$, the peak areas of surface states are 0.13 with p polarized light and 0.09 with s polarized light respectively. And the peak areas of bulk states are 0.47 with p polarized light and 0.25 with s polarized light respectively. Similarly, along $\bar{K}-\bar{\Gamma}-\bar{K}'$, the peak areas of surface states are 0.14 and 0.10 under p and s polarized light, respectively. And the peak areas of bulk states are 0.34 and 0.37 under p and s polarized light, respectively. The corresponding ratios between s and p polarization are 0.692, 0.532, 0.714, and 1.088, respectively, and these values are listed in the middle of Table 2. The photoionization cross section of As4s and As4p orbitals are about 0.2 and 0.1 Mb (1 Mb = 10^{-27} cm²) at $h\nu = 70$ eV respectively²⁹. Assuming that electrons in specific atomic orbitals distribute equally into the molecular orbitals they engage with. Furthermore, as shown in Table 1, the detectability of atomic orbitals depends on high symmetry directions and light polarization. Therefore, the peak area differences in Fig. 5 should be originated from different orbital content of surface and bulk states in grey arsenic.

Comparison of first-principles calculations and ARPES measurements

First-principles calculations were performed to reveal the orbital nature of surface states and bulk states close to the Fermi level in grey arsenic. Figure 6 shows the calculated band structures of grey arsenic (111) along the $\bar{\Gamma}-\bar{M}$ and $\bar{\Gamma}-\bar{K}$ directions, which agree well with the ARPES experimental results. The calculated bulk state band structure considering spin-orbit coupling (SOC) is depicted in Fig. S10. As shown in Fig. 6, we projected band structure to two high-symmetry directions, and both hole pockets donating the bulk states near the Fermi level are contributed by the 4s, 4p_x, 4p_y, and 4p_z orbitals, even if the 4s, 4p_x and 4p_y orbital contributions is weaker than the 4p_z orbital by calculations. Regarding the surface states, the results align with the trends

Table 2 | The measured and predicted orbital ratios between s polarization and p polarization for the surface and bulk states along two high symmetry directions

High symmetry direction	Measured ratio s/p	Predicted ratio s/p
$\bar{M}-\bar{\Gamma}-\bar{M}'$ (Ss)	0.692	0.583
$\bar{M}-\bar{\Gamma}-\bar{M}'$ (Bs)	0.532	0.584
$\bar{K}-\bar{\Gamma}-\bar{K}'$ (Ss)	0.714	0.632
$\bar{K}-\bar{\Gamma}-\bar{K}'$ (Bs)	1.088	0.979

Ss and Bs represent the surface states and bulk states, respectively.

exhibited by the bulk states. Thus, we can unambiguously assert that both the surface and bulk states contain 4s, 4p_x, 4p_y, and 4p_z orbitals.

Additionally, to have more insights into the orbital texture relevant to the ARPES measurements, we have also conducted one-step model of photoemission based on Korringa-Kohn-Rostoker Green's function (KKR) method. The SPR-KKR 8.6 Munich band structure software package was employed as granted by Dr. Ebert. These calculations incorporate the full spin-orbit interaction which are essential for capturing the photoemission response. The calculated photoemission signal includes all matrix element effects such as experimental geometry, photo energy, polarization state, and final state effects. As shown in the Fig. 7, the photoemission anisotropies of grey arsenic are presented along the $\bar{M}-\bar{\Gamma}-\bar{M}'$ and $\bar{K}-\bar{\Gamma}-\bar{K}'$ directions for both p- and s-polarized light. The calculations were performed using the PBE functional and the photon energy is 70 eV. The resulting reveal a clear asymmetry in the band structure along $\bar{\Gamma}-\bar{M}$ ($\bar{\Gamma}-\bar{K}$) and $\bar{\Gamma}-\bar{M}'$ ($\bar{\Gamma}-\bar{K}'$), which is consistent with the experimental observations.

In order to quantitatively predict the orbital difference between the surface states and the bulk states, we calculate the content of 4s, 4p_x, 4p_y, and 4p_z orbitals near the Fermi level along the $\bar{M}-\bar{\Gamma}-\bar{M}'$ and $\bar{K}-\bar{\Gamma}-\bar{K}'$ directions. The selected moment and energy ranges for the surface and bulk states are the same as the scenario in Fig. 4a. The detailed content is shown in Table S1. The 4s and 4p_z orbital content is larger for the surface states than the corresponding values for the bulk states, while the results for 4p_x and 4p_y orbital content are completely opposite. The calculated band structures respectively contain 4s, 4p_x, 4p_y, and 4p_z orbitals along two high-symmetry directions are shown in Fig. S11. According to the s and p polarization dependent detectability of atomic orbitals shown in table1 and the orbital content shown in Table S1, along $\bar{M}-\bar{\Gamma}-\bar{M}'$, the detected orbitals of surface states should be 4s, 4p_x, 4p_y, and 4p_z (the total orbital content equals 1) with p polarized light and 4p_y, and 4p_z (the total orbital content equals 0.583) with s polarized light respectively, thus, the ratio is 0.583. And the detected orbitals of bulk states should be 4s, 4p_x, 4p_y, and 4p_z (the total orbital content equals 1) with p polarized light and 4p_y, and 4p_z (the total orbital content equals 0.584) with s polarized light respectively, and the ratio is 0.584. Correspondingly, along $\bar{K}-\bar{\Gamma}-\bar{K}'$, the detected orbitals of surface states should be 4s, 4p_x, and 4p_z (the total orbital content equals 0.992) with p polarized light and 4p_x, 4p_y, and 4p_z (the total orbital content equals 0.627) with s polarized light respectively, thus, the ratio is 0.632. And the detected orbitals of bulk states should be 4s, 4p_x and 4p_z (the total orbital content equals 0.798) with p polarized light and 4p_x, 4p_y, and 4p_z (the total orbital content equals 0.782) with s polarized light respectively, and the ratio is 0.979. The predicted ratios between p polarized light and s polarized light along the same direction are listed in the right of Table 2.

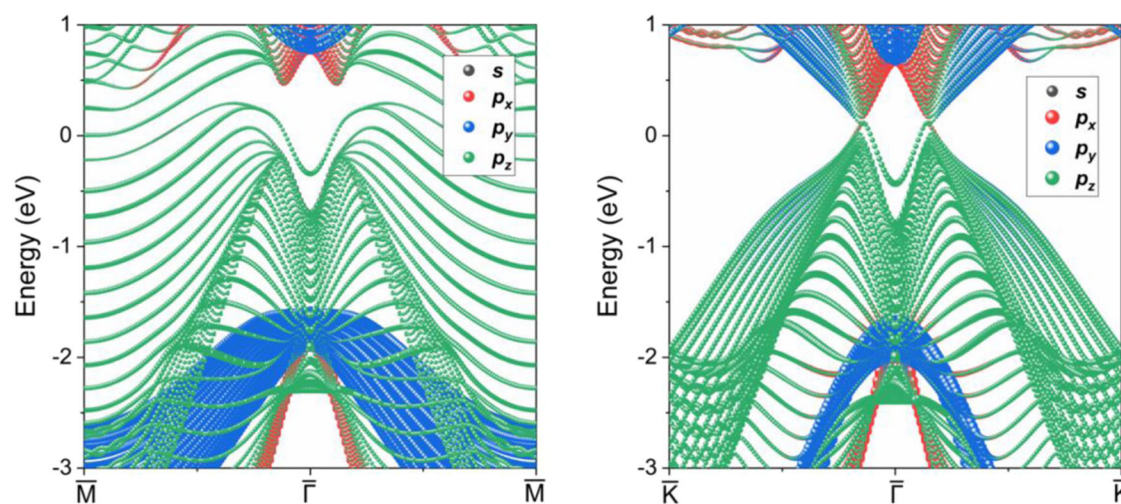


Fig. 6 | Bands along $\bar{M}-\bar{\Gamma}-\bar{K}$ from slab calculations. The band structures along distinct high-symmetry directions exhibit varying orbital components. The s, p_x, p_y and p_z components are shown with red, blue and green colors, respectively.

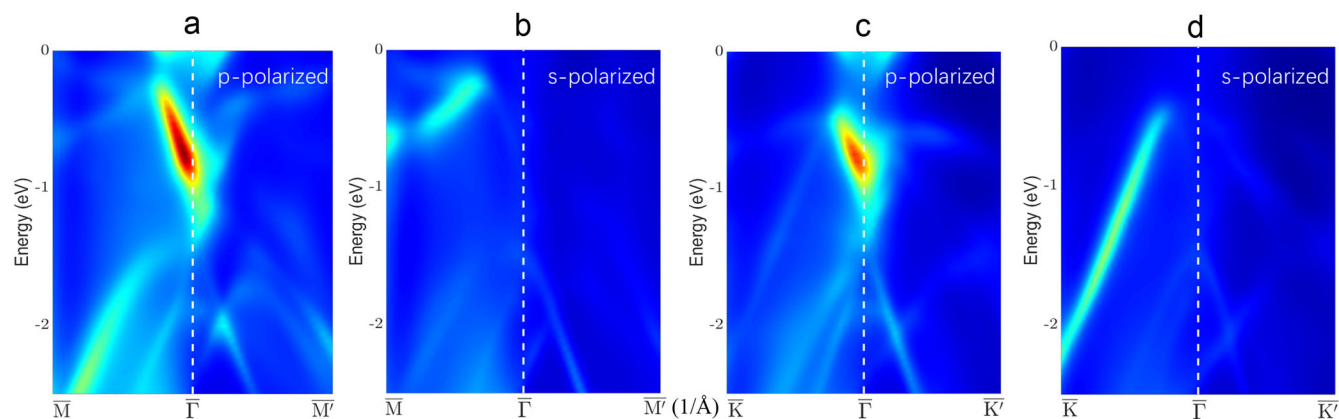


Fig. 7 | Calculated photoemission intensity using the one-step model (KKR) method. Along the M- Γ -M' (a, b) and K- Γ -K' (c, d) with p- and s-polarized light.

Discussion

The predicted ratios under the s polarized light and p polarized light are in good agreement with the experimental results. For the reason of different ratios, one can see the LDAD maps by ARPES. The orbital ratio by theoretical calculation corresponding to the photoemission intensity by the experimental measurements. Via the orbital distributions, one can understand the photoemission intensity difference in different momentum spaces shown in ARPES and Fermi surface maps.

We explore the orbital texture of grey arsenic by means of ARPES together with theoretical calculations. Linear dichroism and corresponding orbital character of bulk and surface bands near the Fermi level are demonstrated under different experimental geometries by rotating the samples and switching the incident light polarizations. The band dispersions and photoemission intensities observed from ARPES experiments along different high-symmetry directions, including \bar{M} - $\bar{\Gamma}$ - \bar{M}' and \bar{K} - $\bar{\Gamma}$ - \bar{K}' , were consistent with the calculations. Both surface and bulk states were found to contain 4s, 4p_x, 4p_y, and 4p_z orbitals. Quantitative analysis of orbital ratios near the Fermi level further distinguished the surface and bulk states, indicating variations in the contributions of 4s, 4p_x, 4p_y, and 4p_z orbitals. Our investigation on the orbital texture provides a universal way to discover linear dichroism properties in other materials and open the possibilities of designing new concept of optoelectronic devices.

Methods

ARPES measurements

ARPES experiments in this work were carried out at Tempo beamline of Synchrotron SOLEIL, France. The photoelectrons were collected with new generation MBS A-1 analyzer, which allows Fermi surface mapping by using mechanical deflection without sample rotation. High-quality single crystals of grey arsenic purchased from “2D Semiconductors” company were cleaved and measured on the (111) plane at base pressure better than 1×10^{-10} mbar and temperature of ~ 80 K. We used two photon energies (70 eV and 120 eV) and different light polarizations (p and s) to probe the samples. In addition, during the measurements, the samples were rotated by 60° with respect to the original geometry in order to investigate the linear dichroism and orbital texture of grey arsenic.

First-principles calculations

First-principles calculations were performed based on the density functional theory (DFT) method as implemented in the Vienna ab initio simulation package (VASP) suite³⁰. The projector augmented wave (PAW)^{31,32} potentials were employed for the electron-core interactions. Exchange-correlation interaction was described by the Perdew-Burke-Ernzerhof (PBE)³³ parametrization of the generalized gradient approximation (GGA). The cutoff energy for the plane-wave basis expansion was set to 500 eV. A convergence criterion of 1×10^{-2} eV/Å for the forces was used during the structural relaxation procedure. The surface states of

As(111) were studied based on the slab model using a $1 \times 1 \times 5$ supercell. The slab of grey arsenic containing 15 As layers was separated from their periodic replicas by 15 Å, and Γ -centered $12 \times 12 \times 11$ k-point meshes were used. For the band structure calculations, spin-orbit coupling (SOC) was considered. The calculations were post-processed by VASPKIT³⁴ package.

Additional calculations

The tight-binding (TB) model calculation for the ARPES and constant energy contour (CEC) were carried out via Chinook code, details of which are discussed in literature³⁵. In this study, we adopted a Slater-Koster type of Hamiltonian, with the basis comprising the arsenic 4s and three 4p (4p_x, 4p_y, and 4p_z) orbitals. The photon energy was set to $h\nu = 120$ eV matching the experimental conditions. SOC was included in the TB calculations and both s-polarized and p-polarized light was considered to account for polarization-dependent effects. Additionally, the one-step model of photoemission was conducted utilizing the spin-polarized-relativistic Korringa-Kohn-Rostoker (SPR-KKR) package based on Green's function and multiple scattering spin-density matrix formalism^{36,37}. The PBE functional was employed for the exchange-correlation potential, and the spin-orbit coupling (SOC) was fully incorporated in the calculation. The ARPES simulations were performed using the same experimental geometry and photon energy, and both s- and p polarization state were considered.

Data availability

The datasets used and/or analyzed during the current study available from the corresponding author on reasonable request.

Code availability

The underlying code for this study is not publicly available but may be made available to qualified researchers on reasonable request from the corresponding author.

Received: 28 June 2024; Accepted: 19 March 2025;

Published online: 27 May 2025

References

- Butler, S. Z. et al. Progress, Challenges, and Opportunities in Two-Dimensional Materials Beyond Graphene. *ACS Nano* **7**, 2898–2926 (2013).
- Khan, K. et al. Recent developments in emerging two-dimensional materials and their applications. *J. Mater. Chem. C* **8**, 387–440 (2020).
- Antonatos, N., Mazanek, V., Lazar, P., Sturla, J. & Sofer, Z. Acetonitrile-assisted exfoliation of layered grey and black arsenic: contrasting properties. *Nanoscale Adv.* **2**, 1282–1289 (2020).
- Hu, Y. et al. 2D Arsenene and Arsenic Materials: Fundamental Properties, Preparation, and Applications. *Small* **18**, 2104556 (2022).

5. Pumera, M. & Sofer, Z. 2D Monoelemental Arsenene, Antimonene, and Bismuthene: Beyond Black Phosphorus. *Adv. Mater.* **29**, 1605299 (2017).
6. Zhang, P. et al. Topologically Entangled Rashba-Split Shockley States on the Surface of Grey Arsenic. *Phys. Rev. Lett.* **118**, 046802 (2017).
7. Cai, X. et al. Quasiparticle interference of the topological surface state on gray arsenic. *Phys. Rev. B* **109**, 035414 (2024).
8. Hossain, M. S. et al. A hybrid topological quantum state in an elemental solid. *Nature* **628**, 527–533 (2024).
9. Manchon, A., Koo, H. C., Nitta, J., Frolov, S. M. & Duine, R. A. New perspectives for Rashba spin-orbit coupling. *Nat. Mater.* **14**, 871–882 (2015).
10. Xu, X., Yao, W., Xiao, D. & Heinz, T. F. Spin and pseudospins in layered transition metal dichalcogenides. *Nat. Phys.* **10**, 343–350 (2014).
11. Zhang, W. et al. Visualizing the evolution from Mott insulator to Anderson insulator in Ti-doped 1T-TaS₂. *Npj Quantum Mater.* **7**, 8 (2022).
12. Schueler, M., Schmitt, T. & Werner, P. Probing magnetic orbitals and Berry curvature with circular dichroism in resonant inelastic X-ray scattering. *Npj Quantum Mater.* **8**, 6 (2023).
13. Koitzsch, A. et al. Intertwined electronic and magnetic structure of the van-der-Waals antiferromagnet Fe₂P₂S₆. *Npj Quantum Mater.* **8**, 27 (2023).
14. Xu, R. Z. et al. Orbital-selective charge-density wave in TaTe₄. *Npj Quantum Mater.* **8**, 44 (2023).
15. Antonelli, T. et al. Orbital-selective band hybridisation at the charge density wave transition in monolayer TiTe₂. *Npj Quantum Mater.* **7**, 98 (2022).
16. Clark, O. J., Dowinton, O., Bahramy, M. S. & Sanchez-Barriga, J. Hidden spin-orbital texture at the (Γ)over-bar-located valence band maximum of a transition metal dichalcogenide semiconductor. *Nat. Commun.* **13**, 4147 (2022).
17. Edwards, B. et al. Giant valley-Zeeman coupling in the surface layer of an intercalated transition metal dichalcogenide. *Nat. Mater.* **22**, 459–465 (2023).
18. Bansil, A. & Lindroos, M. Importance of matrix elements in the ARPES spectra of BISCO. *Phys. Rev. Lett.* **83**, 5154–5157 (1999).
19. Beaulieu, S. et al. Unveiling the orbital texture of 1T-TiTe₂ using intrinsic linear dichroism in multidimensional photoemission spectroscopy. *npj Quantum Mater.* **6**, 93 (2021).
20. Chen, F. et al. The orbital characters of low-energy electronic structure in iron-chalcogenide superconductor K_xFe_{2-y}Se₂. *Chin. Sci. Bull.* **57**, 3829–3835 (2012).
21. Wang, X. P. et al. Orbital characters determined from Fermi surface intensity patterns using angle-resolved photoemission spectroscopy. *Phys. Rev. B* **85**, 214518 (2012).
22. Papalazarou, E. et al. Valence-band electronic structure of V₂O₃: Identification of V and O bands. *Phys. Rev. B* **80**, 155115 (2009).
23. Ohtsubo, Y. et al. Giant Anisotropy of Spin-Orbit Splitting at the Bismuth Surface. *Phys. Rev. Lett.* **109**, 226404 (2012).
24. Zhang, J. et al. Dichroism in time-resolved ARPES and valence band orbital nature in BaNiS₂. *Eur. Phys. J. Spec. Top.* **232**, 2205–2211 (2022).
25. Yoshizawa, K., Yumura, T. & Yamabe, T. A second-order effect causing the layer structure of arsenic. *J. Chem. Phys.* **110**, 11534–11541 (1999).
26. Takayama, A., Sato, T., Souma, S. & Takahashi, T. Rashba effect in antimony and bismuth studied by spin-resolved ARPES. *N. J. Phys.* **16**, 055004 (2014).
27. Beaulieu, S. et al. Revealing Hidden Orbital Pseudospin Texture with Time-Reversal Dichroism in Photoelectron Angular Distributions. *Phys. Rev. Lett.* **125**, 216404 (2020).
28. Scholz, M. R. et al. Reversal of the Circular Dichroism in Angle-Resolved Photoemission from Bi₂Te₃. *Phys. Rev. Lett.* **110**, 216801 (2013).
29. Yeh, J. J. & Lindau, I. Atomic Subshell Photoionization Cross Sections and Asymmetry Parameters: 1 ≤ Z ≤ 103. *At. Data Nucl. Data Tables* **32**, 1–155 (1985).
30. Kresse, G. & Furthmüller, J. Efficient iterative schemes for ab initio total-energy calculations using a plane-wave basis set. *Phys. Rev. B* **54**, 11169–11186 (1996).
31. Blochl, P. E. Projector augmented-wave method. *Phys. Rev. B* **50**, 17953–17979 (1994).
32. Kresse, G. & Joubert, D. From ultrasoft pseudopotentials to the projector augmented-wave method. *Phys. Rev. B* **59**, 1758–1775 (1999).
33. Perdew, J. P., Burke, K. & Ernzerhof, M. Generalized gradient approximation made simple. *Phys. Rev. Lett.* **77**, 3865–3868 (1996).
34. Wang, V., Xu, N., Liu, J.-C., Tang, G. & Geng, W.-T. VASPKIT: A user-friendly interface facilitating high-throughput computing and analysis using VASP code. *Comput. Phys. Commun.* **267**, 108033 (2021).
35. Day, R. P., Zwartsenberg, B., Elfimov, I. S. & Damascelli, A. Computational framework *chironok* for angle-resolved photoemission spectroscopy. *npj Quantum Mater.* **4**, 54 (2019).
36. Ebert, H., Ködderitzsch, D. & Minár, J. Calculating condensed matter properties using the KKR-Green's function method - recent developments and applications. *Rep. Prog. Phys.* **74**, 096501 (2011).
37. Braun, J., Minár, J. & Ebert, H. Correlation, temperature and disorder: Recent developments in the one-step description of angle-resolved photoemission. *Phys. Rep.* **740**, 1–34 (2018).

Acknowledgements

This work is supported by the National Natural Science Foundation of China (Grant No. 22409194), the Energy Revolution S&T Program of Yulin Innovation Institute of Clean Energy, (Grant No. YICE E411060316), the Strategic Priority Research Program of the Chinese Academy of Sciences (Grant No. XDB0600000, XDB0600200) and Natural Science Foundation of Liaoning Province (Grant No. 2024BSBA27).

Author contributions

J.D., J.Z. and Z.Z.: Conceptualization, Experimental Measurements, Investigation, Data curation, Formal analysis, Writing. D. L., Y.Z. and Z.C.: Experimental Measurements, Data curation, Formal analysis. R.L.: performed and interpreted the first-principles calculations. Azzedine Bendounan: Investigation, Data curation, Formal analysis, Reviewing and Editing, Supervision. Z.C.: Conceptualization, Investigation, Data curation, Formal analysis, Reviewing and Editing, Supervision, Funding acquisition. All authors read and approved the final manuscript.

Competing interests

The authors declare no competing interests.

Additional information

Supplementary information The online version contains supplementary material available at <https://doi.org/10.1038/s41535-025-00764-5>.

Correspondence and requests for materials should be addressed to Runze Liu, Azzedine Bendounan or Zhongwei Chen.

Reprints and permissions information is available at <http://www.nature.com/reprints>

Publisher's note Springer Nature remains neutral with regard to jurisdictional claims in published maps and institutional affiliations.

Open Access This article is licensed under a Creative Commons Attribution-NonCommercial-NoDerivatives 4.0 International License, which permits any non-commercial use, sharing, distribution and reproduction in any medium or format, as long as you give appropriate credit to the original author(s) and the source, provide a link to the Creative Commons licence, and indicate if you modified the licensed material. You do not have permission under this licence to share adapted material derived from this article or parts of it. The images or other third party material in this article are included in the article's Creative Commons licence, unless indicated otherwise in a credit line to the material. If material is not included in the article's Creative Commons licence and your intended use is not permitted by statutory regulation or exceeds the permitted use, you will need to obtain permission directly from the copyright holder. To view a copy of this licence, visit <http://creativecommons.org/licenses/by-nc-nd/4.0/>.

© The Author(s) 2025